

RESOLUTION IN DYNAMIC EMISSION TOMOGRAPHY*

JEAN MAEGHT[†] AND DOMINIKUS NOLL[†]

Abstract. Based on a two-dimensional (2-D) Fourier analysis of the attenuated Radon transform and a 2-D version of the Shannon sampling theorem, we investigate the problem of resolution in dynamic emission tomography. As a result we provide guidelines on how to acquire and on how to filter the projection data.

Key words. dynamic emission tomography, photon transport equation, attenuated Radon transform, 2-D sampling theorem, resolution, aliasing errors, uncertainty principle, 2-D filtering

AMS subject classifications. 94A20, 44A12, 92C55

PII. S0036141098345457

1. Introduction. Current state-of-the-art medical imaging technologies provide extremely detailed and accurate information about human anatomy. However, the corresponding detailed information about function is not yet readily available. *Single photon emission computerized tomography* (SPECT) is a noninvasive diagnostic technology which is used to show the blood flow in the heart muscle, extent of damage in stroke patients, presence and degree of malignancy of tumors, and much else.

SPECT is able to image the function of the body through a *tracer*, a biochemical molecule labeled with radioactivity. The radioactive material is incorporated by the patient and metabolized by the organ of interest. The emissions are then recorded by a rotating SPECT camera (cf. Figure 1), and a three-dimensional (3-D) visualization is created from the two-dimensional (2-D) projection data.

Currently, the data recorded by SPECT cameras are static and qualitative. It is not possible, as yet, to measure absolute metabolic rates from the different biological processes, nor to measure the movement of molecules during biodistribution and metabolism. Recently, a major step toward the development of *dynamic* SPECT (dSPECT) has been achieved through two mathematical methods replacing the traditional filtered backprojection (FBP) method (cf. [2, 14, 16, 5]), the latter being by its nature static (cf. [18]) and not feasible for dynamic sources.

The present paper will focus on the problem of resolution in dynamic emission tomography. Results of this type have previously been obtained in static SPECT, in positron emission tomography (PET), and in computed tomography (CT), where an elaborate Fourier analysis led to the idea, among others, of *interlaced grids* which significantly improved resolution (cf. [13, 19, 20, 22]). Following these lines, we shall answer typical questions like how many positions a SPECT camera should take, how long it should stay in a given position, whether views should be recorded over 180 degrees or 360 degrees, or what the internal resolution of the camera should be if a certain spatial resolution in the reconstructed image has to be achieved. As a second application, we present some ideas on how to filter data before doing the actual inversion.

*Received by the editors October 5, 1998; accepted for publication (in revised form) June 23, 1999; published electronically May 2, 2000.

<http://www.siam.org/journals/sima/31-5/34545.html>

[†]Mathématiques pour l'Industrie et la Physique, Université Paul Sabatier, 118 route de Narbonne, 31062 Toulouse, France (maeght@mip.ups-tlse.fr, noll@dumbo.ups-tlse.fr).

2. The model. Emission tomography is modeled by the 3-D dynamic photon transport equation (cf. [8]). It is convenient to simplify the model by assuming that scattering is negligible or, rather, to interpret it as a measurement noise. This decouples the equation and allows for splitting the 3-D reconstruction into a series of 2-D reconstructions on slices. The simplified dynamic 2-D transport equation is

$$(2.1) \quad \frac{1}{c} u_t(t, x, \omega, E) + \omega \cdot \nabla u(t, x, \omega, E) + \mu(x, E) u(t, x, \omega, E) = f(t, x, E),$$

where $u(t, x, \omega, E)$ is the (unknown) photon transport at time t and position $x \in \mathbf{R}^2$ at the energy level E in direction $\omega \in \mathbf{S}^1$, $\mu(x, E)$ is the unknown linear attenuation coefficient at position x for photons traveling with energy E , and $f(t, x, E)$ is the unknown number of photons emitted at time t , position x , at energy level E .

As opposed to X-rays, γ -rays are monochromatic, i.e., photons are emitted at a fixed energy level E_0 , for instance, $E_0 = 140\text{keV}$ for Technetium used in many clinical applications. Similarly, in PET, the recorded photons, originating from the annihilation of a positron with an electron, travel with $E_0 = 511\text{keV}$, the energy of the electron. Photons recorded with energy $E < E_0$ are therefore due to Compton scatter, and an energy window $\pm\Delta E$ about the expected level E_0 allows for eliminating most scattering events (cf. [25]). It is legitimate to further simplify (2.1) by omitting the reference to energy. More precisely, writing $f(t, x, E) = f(t, x) \delta(E - E_0)$ and $\mu(x) = \mu(x, E_0)$, the equation for the cumulative transport $u(t, x, \omega)$ integrated over the relevant energy levels $E \in [E_0 - \Delta E, E_0 + \Delta E]$ is

$$(2.2) \quad \frac{1}{c} u_t(t, x, \omega) + \omega \cdot \nabla u(t, x, \omega) + \mu(x) u(t, x, \omega) = f(t, x),$$

which may be solved explicitly on each line.

To do this, we have to supply boundary conditions. We assume that the unknown source and attenuation coefficient are supported on the unit disk D . We adopt the notations $\omega = (\cos \phi, \sin \phi)$ and $\omega^\perp = (-\sin \phi, \cos \phi)$. Rays may then be referenced (s, ϕ) , that is, $x \cdot \omega^\perp = s$, or $x = s\omega^\perp + \tau\omega$, $\tau \geq 0$ for x on the ray so referenced. Now notice that the incoming radiation is zero, i.e.,

$$u(t, s\omega^\perp + \tau\omega, \omega) = 0 \quad \text{for all } \tau \leq \tau_0 = \tau_0(s, \omega) \text{ and all } t$$

($x_0 = s\omega^\perp + \tau_0\omega$ the entry point of the ray $x \cdot \omega^\perp = s$ into D , if any). Second, we use the fact that $u(t, x, \omega)$ has been recorded at certain times t and for certain directions ω at a camera bin located at $x_1 = s\omega^\perp + \tau_1\omega$, $\tau_1 = \tau_1(s, \omega)$, on the line $x \cdot \omega^\perp = s$. (Without loss, we may assume that x_1 is the exit point of the ray $x \cdot \omega^\perp$ from the disk D , if any.) That is, the observed data are of the form

$$u(t, s\omega^\perp + \tau_1\omega, \omega) =: d(s, \omega, t).$$

In fact, a SPECT camera (shown schematically in Figure 1) detects photons which arrive perpendicular to the camera surface while at a fixed angular position $\omega = (\cos \phi, \sin \phi)$.

Integrating (2.2) using the boundary conditions gives the nonlinear relation

$$(2.3) \quad \int_{\tau_0}^{\tau_1} f(t + (\tau_1 - \tau)/c, s\omega^\perp + \tau\omega) e^{-\int_\tau^{\tau_1} \mu(s\omega^\perp + \rho\omega) d\rho} d\tau = d(s, \omega, t).$$

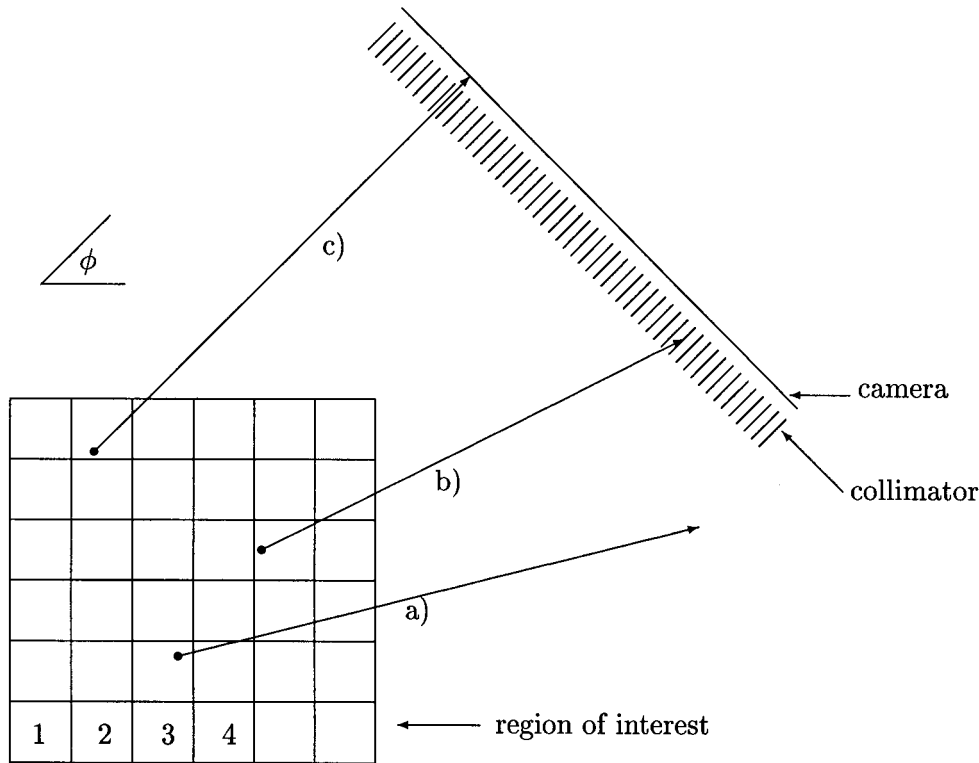


FIG. 1. The principle of SPECT: Photons radiating from the region of interest. (a) Photon misses the camera, (b) is absorbed by the collimator, (c) passes the collimator and hits the camera. The camera rotates around the region of interest (schematically discretized into pixels).

As photons are traveling with the speed of light c , in practice $t + (\tau_1 - \tau_0)/c \approx t$, and (2.3) simplifies to

$$(2.4) \quad R[\mu, f(t, \cdot)](s, \omega) := \int_{\tau_0}^{\tau_1} f(t, s\omega^\perp + \tau\omega) e^{-\int_{\tau}^{\tau_1} \mu(s\omega^\perp + \rho\omega) d\rho} d\tau = d(s, \omega, t).$$

Here $R[\mu, f]$ denotes the *attenuated Radon transform* (cf. [18, 20, 21]). Solving (2.4) simultaneously for the unknown dynamic source $f(t, x)$ and attenuation $\mu(x)$, based on the acquired data $d(s, \omega, t)$, is the mathematical problem of dSPECT. A similar equation replacing (2.4) may be found for PET using the corresponding symmetric data (see [16]).

Attempts to estimate *both* the unknown attenuation and source term from the projection data have been made by several authors. A method proposed by Natterer [18, 21] and reported to be practical in [24] uses a consistency condition to obtain an estimate of μ . This approach is feasible if the camera takes views over 360 degrees and the source is static. More recently, Dicken [9] proposed a direct inversion of (2.4). In practice, often less sophisticated ways are chosen, which consist either in neglecting attenuation or assuming constant attenuation (after tracing the contour of the patient) or in correcting data via some heuristic methods. A third way proposed in [6, 7] consists in doing a CT in parallel with the emission scan. The remaining

problem of estimating f with known μ is then linear but still ill-posed (cf. [20]).

3. Fourier analysis. The way the inverse problem (2.4) is solved depends on the device. A ring SPECT camera, and similarly the PET cameras, allow for collecting a full set of angular views $d(s_j, \omega_k, t_\ell)$, (j the index for camera bins, k the index for angular positions, ℓ the index for stops) at a fixed time t_ℓ . The reconstruction algorithms are then essentially the static ones, FBP or EM algorithms, which reconstruct one static image at a time t_ℓ , obtaining the dynamic image frame by frame. The 2-D Fourier analysis of the static case being known, cf. [20, 13, 22], we may consider this case as essentially understood.

The situation changes if a rotating camera system is used. As the activity in the organ changes significantly during the scan, a rotating camera (even triple head) will not be able to collect sufficiently many views ω_k at a fixed time t_ℓ in order to reconstruct the dynamic object frame by frame. Rather, in the extreme case of a single head camera, we can scan only one position at a time, so the acquired data are $d(s_j, \omega_k, t_k)$. Ideally, the time axis t and angular position ϕ are then linked through

$$(3.1) \quad t = \frac{T}{2\pi} \phi, \quad 0 \leq t \leq T, \quad 0 \leq \phi \leq 2\pi$$

(T is the total acquisition time). With (3.1), reconstruction algorithms necessarily have to process all the projection data simultaneously, which leads to large size problems difficult to solve in practice (cf. [2, 16], and also [12, 5, 10, 14, 17]).

Assuming that the dynamic source is of the form $f(t, x) = g_1(t)h_1(x) + \dots + g_r(t)h_r(x)$, its attenuated Radon transform (2.4) is

$$R[\mu, f(t, \cdot)](s, \phi) = g_1(t)R[\mu, h_1](s, \phi) + \dots + g_r(t)R[\mu, h_r](s, \phi).$$

In the case of a rotating camera, in particular a single head camera, (3.1) leads to the ideal projection data

$$(3.2) \quad p(s, \phi) := g_1((T/2\pi)\phi)R[\mu, h_1](s, \phi) + \dots + g_r((T/2\pi)\phi)R[\mu, h_r](s, \phi),$$

often referred to as the *sinogram* of the source $f(t, x)$, for the obvious reason that a point source scanned over 360 degrees would produce a sinoidal curve. Figures 4(c) and 4(g) show some experimental sinogram data collected over a 180-degree scan.

The principal purpose of the present paper is to perform a 2-D Fourier analysis of the sinogram $p(s, \phi)$. As a result of this analysis we obtain two practical guidelines:

- (1) On *resolution*. How many stops and angular positions are required to capture a prescribed spatial resolution along with a predicted half-life? How long should an individual stop last?
- (2) On *data filtering*, which is inherent to the classical FBP algorithms but has to be considered anew in dSPECT.

4. Sampling in two-dimensions. In this section, we shall be concerned with the sampling of the sinogram (3.2) of a dynamic source $f(t, x)$. In the first round we shall consider only the unattenuated Radon transform (i.e., $\mu = 0$). Later on we will indicate that the results are usually not altered if attenuation is taken into account.

We recall that the Radon transform $Rh(s, \phi)$ of a spatial function $h(x)$, being 2π -periodic in ϕ , is defined on $\mathbf{R} \times \mathbf{S}^1$, which we shall call the (s, ϕ) -plane or *physical plane*. The 2-D Fourier transform \hat{p} of $p(s, \phi)$ is then defined on $\mathbf{R} \times \mathbf{Z}$, which will be referred to as the (σ, k) -plane or *frequency plane*.

A sampling operator $\mathcal{S}_{K,W}$ in the physical plane is defined by two ingredients—a *sampling lattice* $W\mathbf{Z}^2$ in the physical plane (W a 2×2 -matrix) in tandem with a *spectral window* K in the frequency plane—whose replica $K + 2\pi(W^{-1})^T \ell$, $\ell \in \mathbf{Z}^2$, generated by the *dual lattice* $2\pi(W^{-1})^T \mathbf{Z}^2$ in the frequency-plane, are mutually disjoint:

$$(4.1) \quad \mathcal{S}_{K,W}p(s, \phi) := \det(W) \sum_{\ell \in \mathbf{Z}^2} p(W\ell) \hat{\chi}_K((s, \phi) - W\ell)$$

(χ_K the characteristic function of the set K). More formally, $\mathcal{S}_{K,W}$ may be represented using the shah-distribution $\mathbb{I}\mathbb{I}(s, \phi) = \sum_{\ell \in \mathbf{Z}^2} \delta(s - \ell_1, \phi - \ell_2)$,

$$\mathcal{S}_{K,W}p = \left(p \cdot \mathbb{I}\mathbb{I}(W^{-1}\cdot) \right) * \hat{\chi}_K,$$

a formulation which is very intuitive when we consider its Fourier transform. Replacing the analog signal p by its digitized version $p \cdot \mathbb{I}\mathbb{I}(W^{-1}\cdot)$, taken at the points of the lattice $W\mathbf{Z}^2$, has the following effect: Since $\mathbb{I}\mathbb{I} = \widehat{\mathbb{I}\mathbb{I}}$, the spectrum of the digitized signal shows the true spectrum, \hat{p} , but repeated periodically

$$\left(p \cdot \mathbb{I}\mathbb{I}(W^{-1}\cdot) \right)^\wedge = 2\pi \sum_{\ell \in \mathbf{Z}^2} \hat{p}(\cdot - 2\pi W^{-T} \ell)$$

along the dual lattice $2\pi W^{-T} \mathbf{Z}^2$. Consequently, if the spectral window K is well chosen, i.e., if the spectrum \hat{p} is captured by K , we may fully retrieve the true signal p , simply by applying an ideal low pass filter χ_K which eliminates frequencies $\notin K$:

$$(4.2) \quad (\mathcal{S}_{K,W}p)^\wedge = (2\pi)^{-1} \left(p \cdot \mathbb{I}\mathbb{I}(W^{-1}\cdot) \right)^\wedge \cdot \chi_K = \sum_{\ell \in \mathbf{Z}^2} \hat{p}(\cdot - 2\pi W^{-T} \ell) \cdot \chi_K.$$

In fact, 2-D versions of the Shannon sampling theorem are easily understood through (4.2): the signal p is fully retrieved from the sampled signal if its spectrum has $\text{supp}(\hat{p}) \subset K$. In our applications, however, we are dealing with compactly supported signals, whose spectra \hat{p} are analytic and never fully supported on a bounded set K . We will consequently have to accept aliasing errors associated with the choice of a sampling operator (4.1). Estimating these errors is the principal task of the present section. Practical aspects will be considered later.

Let us fix $0 < \vartheta < 1$, a positive integer m , and $b > 0$. As our frequency window in the (σ, k) -plane we choose the *bowtie region* K ,

$$(4.3) \quad K = \{(\sigma, k) \in \mathbf{R} \times \mathbf{Z} : |\sigma| \leq b \text{ and } |k| \leq |\sigma|/\vartheta + m\},$$

which is displayed in Figure 2(a). Figure 2(c) indicates the scheme $2\pi W^{-T} \mathbf{Z}^2$ which produces nonoverlapping replica of K in the frequency plane. The sampling parameters are seen to be $\Delta k = [b/\vartheta] + 2m$ and $\Delta \sigma = b$, and the matrices W , $2\pi W^{-T}$ are

$$(4.4) \quad W = 2\pi \begin{pmatrix} \frac{1}{2b} & 0 \\ -\frac{1}{2\Delta k} & \frac{1}{\Delta k} \end{pmatrix}, \quad 2\pi(W^{-1})^T = \begin{pmatrix} 2b & b \\ 0 & \Delta k \end{pmatrix}.$$

As we shall see in our experiments, the parameter ϑ may in practice be chosen as $\vartheta \approx 1$ but for theoretical reasons has to satisfy $\vartheta \in (0, 1)$.

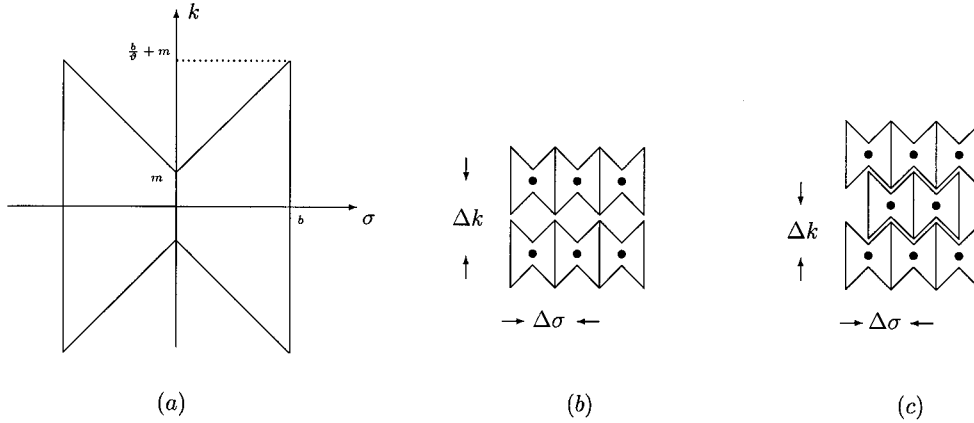


FIG. 2. (a) shows the bowtie region K defined through (4.3), (4.4), while (b) and (c) show two different lattices generating disjoint replica of K . The interlaced grid (c) requires fewer nodes and therefore gives a better sampling scheme.

Naturally, the identification of the essential support K of the spectrum \hat{p} in tandem with the sampling lattice $W\mathbf{Z}^2$ is crucial for our principal tasks: resolution and filtering. The choice of K being ambiguous, we shall have to support our proposition (4.3) both by numerical tests and by a rigorous analysis, including error estimates. In the present section we proceed to provide those.

To formulate our main result, we need to introduce two notions for the spatial and temporal bandwidths, respectively. Concerning the spatial term, Natterer [20] considers the measures

$$\epsilon_d(h, b) = \int_{|\xi|>b} |\xi|^d |\hat{h}(\xi)| d\xi,$$

which may be related to appropriate Sobolev norms. In fact, using

$$\|h\|_{W^{\alpha,d}} = \left(\int_{\mathbf{R}^n} (1 + |\xi|^2)^{d\alpha/2} |\hat{h}(\xi)|^\alpha d\xi \right)^{1/\alpha},$$

and defining the ideal *high pass filter at frequency b* , \mathcal{H}_b , via $(\mathcal{H}_b h)^\wedge = \hat{h} \chi_{\{|\cdot|>b\}}$, Natterer’s error terms satisfy $C_1 \epsilon_d(h, b) \leq \|\mathcal{H}_b h\|_{W^{1,d}} \leq C_2 \epsilon_d(h, b)$. For the following we shall, in addition, obtain error estimates involving the Hilbert space norms $\|\mathcal{H}_b h\|_{W^{2,d}}$.

In turn, for a 2π -periodic function $g(\phi)$ with Fourier coefficients \hat{g}_k , low pass filtering at a frequency k obviously corresponds to truncating the Fourier series at k , and correspondingly, high pass filtering corresponds to retaining the tail $|\nu| > k$ of the series. We therefore consider the error terms

$$R_k(g) := \left(\sum_{|\nu|>k} |\hat{g}_\nu|^2 \right)^{1/2},$$

$k > 0$, which play a role similar to the norm estimates of $\mathcal{H}_b h$ above. With these notions we are ready to state the following theorem.

THEOREM 4.1. *Let ϑ, m, b and K, W be as in (4.3), (4.4). Choose $\vartheta' \in (\vartheta, 1)$, and let $\theta := \vartheta/\vartheta' \in (0, 1)$. Consider a dynamic source of the form $f(t, x) = g(t)h(x)$ such*

that $h(x)$ is continuous and supported on the unit disk D and $g(t)$ is continuous. Let $g((T/2\pi)\phi)$ be continued periodically for $\phi \notin [0, 2\pi]$. Let $p(s, \phi)$ be the ideal sinogram of $f(t, x)$, and let $\mathcal{S}_{K,Wp}(s, \phi)$ be the sinogram sampled on the lattice $W\mathbf{Z}^2$ in the (s, ϕ) -plane using the frequency window K . Then

$$\begin{aligned}
 1. \quad \|p - \mathcal{S}_{K,Wp}\|_\infty &= \|g\|_\infty \mathcal{O}\left(m\epsilon_{-1}(h, b) + \epsilon_0(h, b)\right) \\
 &\quad + \|h\|_\infty \mathcal{O}\left(\sum_{\nu=1}^\infty \nu R_{(1-\vartheta')(\nu+m)}(g)\right), \\
 2. \quad \|p - \mathcal{S}_{K,Wp}\|_2 &= \|g\|_\infty \mathcal{O}\left(\|\mathcal{H}_b h\|_{W^{2,-\frac{1}{2}}}\right) \\
 &\quad + \|h\|_\infty \mathcal{O}\left(\left(\sum_{\nu=1}^\infty \nu R_{(1-\vartheta')(\nu+m)}(g)^2\right)^{1/2}\right), \\
 3. \quad \|p - \mathcal{S}_{K,Wp}\|_2 &= \|g\|_\infty \mathcal{O}\left(\|\mathcal{H}_b h\|_{W^{2,-\frac{1}{2}}}\right) \\
 &\quad + \|h\|_\infty \mathcal{O}\left(b^{1/2} \left(\sum_{\nu=1}^\infty R_{(1-\vartheta')(\nu+m)}(g)^2\right)^{1/2}\right).
 \end{aligned}$$

Proof. Part 1. Notice that by Parseval’s formula, $\|p\|_2 = \|\hat{p}\|_2$, where \hat{p} is the 2-D Fourier transform of p , and according to [20, p. 63], $\|p\|_\infty \leq \|\hat{p}\|_1$, if the corresponding norms on the frequency plane are defined through

$$(4.5) \quad \|\hat{p}\|_\alpha = \left(\sum_{k=-\infty}^\infty \int_{\mathbf{R}} |\hat{p}(\sigma, k)|^\alpha d\sigma\right)^{1/\alpha}.$$

By the definition of the sampling operator (4.1),

$$\hat{p} - (\mathcal{S}_{K,Wp})^\wedge = (1 - \chi_K)\hat{p} - \sum_{\ell \neq 0} \hat{p}(\cdot - 2\pi W^{-T}\ell)\chi_K,$$

so we derive the estimate

$$\|(p - \mathcal{S}_{K,Wp})^\wedge\|_\alpha \leq \|(1 - \chi_K)\hat{p}\|_\alpha + \left\| \sum_{\ell \neq 0} \hat{p}(\cdot - 2\pi W^{-T}\ell)\chi_K \right\|_\alpha.$$

By the translation invariance of the Haar measure and using the fact that the translates $K + 2\pi W^{-T}\ell$ are disjoint, the second term on the right-hand side satisfies

$$\left\| \sum_{\ell \neq 0} \hat{p}(\cdot - 2\pi W^{-T}\ell)\chi_K \right\|_\alpha \leq \|(1 - \chi_K)\hat{p}\|_\alpha,$$

so all together

$$\|(p - \mathcal{S}_{K,Wp})^\wedge\|_\alpha \leq 2\|(1 - \chi_K)\hat{p}\|_\alpha.$$

Writing $K(k) = \{\sigma : (\sigma, k) \in K\}$, we are therefore led to estimate

$$(4.6) \quad \sum_{k=-\infty}^\infty \int_{\sigma \notin K(k)} |\hat{p}(\sigma, k)|^\alpha d\sigma.$$

To do this, we will have to distinguish the cases $\alpha = 1$ and $\alpha = 2$. For the case $\alpha = 1$, we decompose the region $(\sigma, k) \notin K$ into three parts Σ_1, Σ_2 , and Σ_3 :

$$\begin{aligned} \Sigma_1 &= \{(\sigma, k) : |k| > |\sigma|/\vartheta + m\}, \\ \Sigma_2 &= \{(\sigma, k) : |\sigma| > b \text{ and } |k| \leq b/\vartheta + m\}, \\ \Sigma_3 &= \{(\sigma, k) : |\sigma| > b \text{ and } |k| \leq |\sigma|/\vartheta + m \text{ and } |k| \geq b/\vartheta + m\}. \end{aligned}$$

For the case $\alpha = 2$, two domains Γ_1, Γ_2 will do:

$$\begin{aligned} \Gamma_1 &= \{(\sigma, k) : |k| \geq m \text{ and } |\sigma| \leq \min(b, \vartheta(|k| - m))\}, \\ \Gamma_2 &= \{(\sigma, k) : |\sigma| > b\}. \end{aligned}$$

Part 2. Let us continue collecting useful information. Let $\mathcal{F}_s p(\cdot, \phi)(\sigma)$ be the one-dimensional (1-D) Fourier transform of p with respect to s , which is again 2π -periodic in ϕ . Its k th Fourier coefficient is

$$\hat{p}(\sigma, k) =: \hat{p}_k(\sigma) = \frac{1}{2\pi} \int_0^{2\pi} \mathcal{F}_s p(\sigma, \phi) e^{-ik\phi} d\phi.$$

By the Fourier slice theorem [20, p. 11] we have

$$\mathcal{F}_s p(\sigma, \phi) = g((T/2\pi)\phi) \mathcal{F}_s [Rh(\cdot, \phi)](\sigma) = g((T/2\pi)\phi) \hat{h}(\sigma\omega)$$

with $\omega = (\cos \phi, \sin \phi)$. Then

$$\begin{aligned} (4.7) \quad \hat{p}_k(\sigma) &= (2\pi)^{-1/2} \int_0^{2\pi} g((T/2\pi)\phi) \hat{h}(\sigma\omega) e^{-ik\phi} d\phi \\ &= (2\pi)^{-3/2} \int_0^{2\pi} g((T/2\pi)\phi) \int_D e^{-i\sigma\omega \cdot x} h(x) dx e^{-ik\phi} d\phi \\ &= (2\pi)^{-3/2} \int_D h(x) \int_0^{2\pi} g((T/2\pi)\phi) e^{-i\sigma|x|\cos(\phi-\psi) - ik\phi} d\phi dx \end{aligned}$$

if we put $x = |x|(\cos \psi, \sin \psi)$. Substituting the Fourier series $g((T/2\pi)\phi) = \sum_\nu \hat{g}_\nu e^{i\nu\phi}$, this becomes

$$\begin{aligned} (4.8) \quad \hat{p}_k(\sigma) &= (2\pi)^{-3/2} \int_D h(x) e^{-ik\psi} \sum_{\nu=-\infty}^{\infty} \hat{g}_\nu \int_0^{2\pi} e^{-i\sigma|x|\cos\phi - i(k-\nu)\phi} d\phi dx \\ &= (2\pi)^{-1/2} i^k \int_D h(x) e^{-ik\psi} \sum_{\nu=-\infty}^{\infty} \hat{g}_\nu J_{k-\nu}(-\sigma|x|) dx, \end{aligned}$$

where we have used the Bessel functions $J_k(x)$ of the first kind defined through

$$J_k(x) = \frac{i^{-k}}{2\pi} \int_0^{2\pi} e^{ix \cos \phi - ik\phi} d\phi.$$

Part 3. Let us now consider the estimate on Σ_2 with $\alpha = 1$. As a consequence of (4.7),

$$\begin{aligned} (4.9) \quad \int_{|\sigma|>b} |\hat{p}_k(\sigma)| d\sigma &\leq (2\pi)^{-1/2} \|g\|_\infty \int_{|\sigma|>b} \int_0^{2\pi} |\hat{h}(\sigma\omega)| d\phi d\sigma \\ &= (2\pi)^{-1/2} \|g\|_\infty \int_{|\xi|>b} \frac{|\hat{h}(\xi)|}{|\xi|} d\xi = (2\pi)^{-1/2} \|g\|_\infty \epsilon_{-1}(h, b). \end{aligned}$$

Now observe that $(\sigma, k) \in \Sigma_2$ only for $|k| \leq b/\vartheta + m$, so we are left with a finite number of terms (4.9). In fact

$$\begin{aligned} \|\chi_{\Sigma_2} \hat{p}\|_1 &= \sum_{|k| \leq b/\vartheta + m} \int_{|\sigma| > b} |\hat{p}_k(\sigma)| d\sigma \leq C \|g\|_\infty (2b/\vartheta + 2m + 1) \epsilon_{-1}(h, b) \\ (4.10) \quad &\leq C \|g\|_\infty (b\epsilon_{-1}(h, b) + m\epsilon_{-1}(h, b)) \leq C \|g\|_\infty (\epsilon_0(h, b) + m\epsilon_{-1}(h, b)), \end{aligned}$$

where the last inequality uses (2.9) in [20, p. 66].

Part 4. Let us next discuss the estimate on Σ_3 , $\alpha = 1$. According to (4.9) above, replacing b by $\vartheta(|k| - m)$ gives

$$\int_{|\sigma| \geq \vartheta(|k| - m)} |\hat{p}_k(\sigma)| d\sigma \leq C \|g\|_\infty \epsilon_{-1}(h, \vartheta(|k| - m)).$$

But then

$$\begin{aligned} \|\chi_{\Sigma_3} \hat{p}\|_1 &= \sum_{|k| \geq b/\vartheta + m} \int_{|\sigma| \geq \vartheta(|k| - m)} |\hat{p}_k(\sigma)| d\sigma \\ (4.11) \quad &\leq C \|g\|_\infty \sum_{|k| \geq b/\vartheta + m} \epsilon_{-1}(h, \vartheta(|k| - m)) \leq C \|g\|_\infty \epsilon_0(h, b), \end{aligned}$$

where the last inequality again uses (2.9) in [20, p. 66].

Part 5. Let us catch up with the error estimate on Γ_2 , $\alpha = 2$. Using (4.7), for fixed σ , and with $\omega = (\cos \phi, \sin \phi)$, Parseval's equality gives

$$\sum_{k=-\infty}^{\infty} |\hat{p}_k(\sigma)|^2 = \int_0^{2\pi} |g((T/2\pi)\phi) \hat{h}(\sigma\omega)|^2 d\phi.$$

Integrating over $|\sigma| > b$ shows

$$\begin{aligned} \|\chi_{\Gamma_2} \hat{p}\|_2^2 &\leq C \|g\|_\infty^2 \int_{|\sigma| > b} \int_0^{2\pi} |\hat{h}(\sigma\omega)|^2 d\phi d\sigma \\ (4.12) \quad &= C \|g\|_\infty^2 \int_{|\xi| > b} \frac{|\hat{h}(\xi)|^2}{|\xi|} d\xi \leq C \|g\|_\infty^2 \|\mathcal{H}_b h\|_{W^{2, -\frac{1}{2}}}^2. \end{aligned}$$

Part 6. We need to consider some technical preliminaries about Bessel functions. It is well known that $J_n(\sigma)$ decays exponentially ($n \rightarrow \infty$) for fixed σ . According to [23] even $J_n(\theta n) \rightarrow 0$ exponentially, since $0 < \theta < 1$. We'll improve this by showing that, regarding $0 < \theta < 1$, $R_n(J(\theta n)) \rightarrow 0$ exponentially as $n \rightarrow \infty$.

According to [23, p. 255] in tandem with [1, Theorem 4.1.28], and regarding $0 < \theta < 1$, we have (for n a positive integer)

$$0 \leq J_n(\theta n) \leq (2\pi n)^{-1/2} (1 - \theta^2)^{-1/4} e^{-(n/3)(1 - \theta^2)^{3/2}}.$$

Summing over $|\nu| \geq n$ and using $|J_\nu(-\sigma)| = |J_\nu(\sigma)|$, $|J_{-\nu}(\sigma)| = |J_\nu(\sigma)|$ gives

$$\begin{aligned} \sum_{|\nu| \geq n} |J_\nu(\theta n)|^2 &= 2 \sum_{\nu=n}^{\infty} |J_\nu((\theta n/\nu) \cdot \nu)|^2 \\ &\leq 2 \sum_{\nu=n}^{\infty} \left((2\pi\nu)^{-1/2} (1 - (\theta n/\nu)^2)^{-1/4} e^{-(\nu/3)(1 - (\theta n/\nu)^2)^{3/2}} \right)^2. \end{aligned}$$

This term is easily seen to decay exponentially in n , that is,

$$(4.13) \quad |R_n(J.(\theta'n))| \leq C e^{-c(\theta)n}$$

for a constant $c(\theta) > 0$ depending on θ , and uniformly over $0 \leq \theta' \leq \theta$.

Part 7. Let us now consider the error estimates on Σ_1 with $\alpha = 1$. Writing

$$d_k(\sigma) := \sum_{\nu=-\infty}^{\infty} \hat{g}_\nu J_{k-\nu}(\sigma) = (\hat{g} * J.(\sigma))_k \quad (\text{convolution of sequences}),$$

we find using (4.8) that

$$(4.14) \quad |\hat{p}_k(\sigma)| \leq C \|h\|_\infty \max_{|x| \leq 1} d_k(-\sigma|x|),$$

and by the definition of Σ_1 , we are led to estimate $d_k(-\sigma|x|)$ for $|\sigma| \leq \vartheta(|k| - m)$, $|k| \geq m$, and $|x| \leq 1$. This is done by the following steps. Observe that

$$\begin{aligned} |d_k(-\sigma|x|)| &\leq \sum_{\nu=-\infty}^{\infty} |\hat{g}_\nu J_{k-\nu}(-\sigma|x|)| \\ &= \sum_{|\nu| \geq (1-\vartheta')|k|} |\hat{g}_\nu J_{k-\nu}(-\sigma|x|)| + \sum_{|\nu| < (1-\vartheta')|k|} |\hat{g}_\nu J_{k-\nu}(-\sigma|x|)| =: \text{I} + \text{II}. \end{aligned}$$

The first term I satisfies

$$(4.15) \quad \text{I} \leq \left(\sum_{|\nu| \geq (1-\vartheta')|k|} |\hat{g}_\nu|^2 \right)^{1/2} \left(\sum_{|\nu| \geq (1-\vartheta')|k|} |J_{k-\nu}(-\sigma|x|)|^2 \right)^{1/2} \leq R_{(1-\vartheta')|k|}(g),$$

the second factor being ≤ 1 since $\sum_k |J_k(z)|^2 = 1$ for every z . The second term II is estimated through

$$(4.16) \quad \text{II} \leq \|g\|_2 \left(\sum_{|\nu| < (1-\vartheta')|k|} |J_{k-\nu}(-\sigma|x|)|^2 \right)^{1/2} \leq \|g\|_2 R_{\vartheta'|k|}(J.(-\sigma|x|)).$$

Here the argument $-\sigma|x|$ of the Bessel coefficients satisfies

$$|-\sigma|x|| \leq |\sigma| \leq \vartheta(|k| - m) = \vartheta'|k| \frac{\vartheta(|k| - m)}{\vartheta'|k|} \leq \vartheta'|k| \cdot \frac{\vartheta}{\vartheta'} = \vartheta'|k| \cdot \theta,$$

which means that $|-\sigma|x|| = \theta'\vartheta'|k|$ for some $0 \leq \theta' \leq \theta$. The latter allows us to apply (4.13) with $n = \vartheta'|k|$:

$$(4.17) \quad R_{\vartheta'|k|}(J.(-\sigma|x|)) \leq C e^{-\gamma(\theta)|k|} \quad \text{for } |\sigma| \leq \vartheta(|k| - m)$$

and some $\gamma(\theta) > 0$.

Finally, using in this order (4.14), (4.15), (4.16), and (4.17), the error term on Σ_1 is

$$\begin{aligned} \|\chi_{\Sigma_1} \hat{p}\|_1 &\leq C \|h\|_\infty \max_{|x| \leq 1} \sum_{|k| \geq m} \int_{|\sigma| \leq \vartheta(|k| - m)} |d_k(-\sigma|x|)| d\sigma \\ &\leq C \|h\|_\infty \sum_{|k| \geq m} (|k| - m) \left(R_{(1-\vartheta')|k|}(g) + \|g\|_2 e^{-\gamma(\theta)|k|} \right) \\ (4.18) \quad &\leq C \|h\|_\infty \left(\sum_{\nu=1}^{\infty} \nu R_{(1-\vartheta')(\nu+m)}(g) + \|g\|_2 e^{-\delta(\theta)m} \right) \end{aligned}$$

for another constant $\delta(\theta) > 0$. Clearly then, (4.18) shows us that $\|\chi_{\Sigma_1}\hat{p}\|_1 = \|h\|_\infty \mathcal{O}(\sum_{\nu=1}^\infty \nu R_{(1-\vartheta')(\nu+m)}(g))$, the exponentially decaying term being negligible. Combining this with (4.10) and (4.11) gives statement 1.

Part 8. Our last step is the error estimate $\|\chi_{\Gamma_1}\hat{p}\|_2$. Notice that by the definition of Γ_1 ,

$$\begin{aligned} \|\chi_{\Gamma_1}\hat{p}\|_2^2 &\leq \sum_{|k|\geq m} \int_{|\sigma|\leq \min\{b, \vartheta(|k|-m)\}} |\hat{p}_k(\sigma)|^2 d\sigma \\ &\leq \sum_{m\leq |k|\leq \frac{b}{\vartheta}+m} \int_{|\sigma|\leq \vartheta(|k|-m)} |\hat{p}_k(\sigma)|^2 d\sigma + \sum_{|k|\geq \frac{b}{\vartheta}+m} \int_{|\sigma|\leq b} |\hat{p}_k(\sigma)|^2 d\sigma =: \text{III}^2 + \text{IV}^2. \end{aligned}$$

Using (4.14) and (4.17), we find

$$\begin{aligned} \text{III}^2 &\leq C \|h\|_\infty^2 \max_{|x|\leq 1} \sum_{m\leq |k|\leq \frac{b}{\vartheta}+m} \int_{|\sigma|\leq \vartheta(|k|-m)} |d_k(-\sigma|x)|^2 d\sigma \\ &\leq C \|h\|_\infty^2 \sum_{m\leq |k|\leq \frac{b}{\vartheta}+m} \int_{|\sigma|\leq \vartheta(|k|-m)} \left(R_{(1-\vartheta')|k|}(g) + \|g\|_2 e^{-\delta|k|} \right)^2 d\sigma, \end{aligned}$$

(4.17) being applicable since $|\sigma|x| \leq \vartheta(|k|-m) < \vartheta'|k|$. By the triangle inequality, and on setting $\nu = |k| - m$,

$$\text{III} \leq C \|h\|_\infty \left(\left(\sum_{\nu=1}^{b/\vartheta} \nu R_{(1-\vartheta')(\nu+m)}(g)^2 \right)^{1/2} + \|g\|_2 e^{-\gamma m} \right)$$

for another constant $\gamma > 0$. Similarly, the term IV satisfies

$$\text{IV} \leq C \|h\|_\infty \left(b^{1/2} \left(\sum_{\nu=b/\vartheta}^\infty R_{(1-\vartheta')(\nu+m)}(g)^2 \right)^{1/2} + \|g\|_2 e^{-\delta m} \right).$$

So all together,

$$\|\chi_{\Gamma_1}\hat{p}\|_2 \leq C \|h\|_\infty \left(\left(\sum_{\nu=1}^\infty \min\{\nu, b\} R_{(1-\vartheta')(\nu+m)}(g)^2 \right)^{1/2} + \|g\|_2 e^{-\delta m} \right),$$

which in tandem with (4.12) responds to estimates 2 and 3, again since the exponentially decaying term is negligible. \square

The function $h(x)$, supported on the unit disk D , is called *essentially bandlimited* if

$$\epsilon_0(h, b) = \int_{|\xi|>b} |\hat{h}(\xi)| d\xi \leq C e^{-\gamma b}$$

for certain $C > 0, \gamma > 0$. Equivalently, this means that $\|\mathcal{H}_b h\|_1$ decays exponentially as $b \rightarrow \infty$. By Hölder's inequality

$$\|\mathcal{H}_b h\|_{W^{2,-\frac{1}{2}}} \leq \|\hat{h}\|_\infty^{1/2} \|\mathcal{H}_b h\|_1^{1/2} \leq C e^{-\gamma b/2},$$

so for an essentially bandlimited function $h(x)$, $\|\mathcal{H}_b h\|_{W^{2,-\frac{1}{2}}}$ also decays exponentially (as $b \rightarrow \infty$).

COROLLARY 4.2. *With the same notations as in the theorem, suppose that $b \rightarrow \infty, m \rightarrow \infty$, and either $m = \mathcal{O}(b)$ or $b = \mathcal{O}(m)$. Let $h(x)$ be essentially bandlimited. Then*

1. $\hat{g}_k = \mathcal{O}(|k|^{-\rho})$ for some $\rho > \frac{5}{2}$ implies $\|p - \mathcal{S}_{K,Wp}\|_\infty = \mathcal{O}(m^{\frac{5}{2}-\rho}) \rightarrow 0$.
2. $\hat{g}_k = \mathcal{O}(|k|^{-\rho})$ for some $\rho > \frac{3}{2}$ implies $\|p - \mathcal{S}_{K,Wp}\|_2 = \mathcal{O}(m^{\frac{3}{2}-\rho}) \rightarrow 0$.
3. $\hat{g}_k = \mathcal{O}(|k|^{-\rho})$ for some $\rho > 1$ implies $\|p - \mathcal{S}_{K,Wp}\|_2 = \mathcal{O}(b^{\frac{1}{2}}m^{1-\rho})$.

Proof. Suppose $m = \mathcal{O}(b)$; then $m\epsilon_{-1}(h, b) = \mathcal{O}(b\epsilon_{-1}(h, b)) = \mathcal{O}(\epsilon_0(h, b))$. Similarly if $b = \mathcal{O}(m)$, then $m\epsilon_{-1}(h, b) = m\epsilon_{-1}(h, \mathcal{O}(m)) = \mathcal{O}(\epsilon_0(h, m))$. This shows that the terms involving $\epsilon_d(h, b)$ and $\|\mathcal{H}_b h\|_{W^{2,-\frac{1}{2}}}$ in Theorem 4.1 decay exponentially, and we are left with the error terms related to g .

To estimate these, observe that for $\rho > 1$, $\hat{g}_k = \mathcal{O}(|k|^{-\rho})$ gives $R_k(g) = \mathcal{O}(|k|^{-\rho+\frac{1}{2}})$. Then

$$R_m[R_{(1-\vartheta')\cdot}(g)] = \mathcal{O}(m^{-\rho+1}),$$

which, using statement 3 in Theorem 4.1, gives the estimate 3. Similarly, if $\rho > 3/2$, then

$$\left(\sum_{\nu=1}^{\infty} \nu R_{(1-\vartheta')(\nu+m)}(g)^2\right)^{1/2} = \mathcal{O}\left(\left(\sum_{\nu=1}^{\infty} \nu(\nu+m)^{-2\rho+1}\right)^{1/2}\right) = \mathcal{O}(m^{-\rho+\frac{3}{2}}) \rightarrow 0,$$

which, using statement 2 in Theorem 4.1, provides estimate 2.

Finally, for $\rho > \frac{5}{2}$, $R_k(g) = \mathcal{O}(|k|^{-\rho+\frac{1}{2}})$ gives

$$\sum_{\nu=1}^{\infty} \nu R_{(1-\vartheta')(\nu+m)}(g) = \mathcal{O}\left(\sum_{\nu=1}^{\infty} \nu(\nu+m)^{-\rho+\frac{1}{2}}\right) = \mathcal{O}(m^{\frac{5}{2}-\rho}),$$

as claimed in statement 1. \square

The estimates 1–3 do not include the case $\hat{g}_k = \mathcal{O}(|k|^{-1})$, as $R_{(1-\vartheta')(\nu+m)}(g)$ is then no longer well behaved. This may be overcome by considering different norms, as we proceed to do. For $1 < \alpha' < 2$ and $1/\alpha + 1/\alpha' = 1$, define a norm $|\cdot|_{\alpha'}$ on the physical plane by

$$|p|_{\alpha'} := \|\hat{p}\|_{\alpha} = \left(\sum_{k=-\infty}^{\infty} \int_{\mathbf{R}} |\hat{p}(\sigma, k)|^{\alpha} d\sigma\right)^{1/\alpha},$$

which is in accordance with the norms $\|\hat{p}\|_{\alpha}$ for $\alpha = 1, 2$ employed before. Notice that for $1 < \alpha' < 2$ these norms are less natural than the classical norms $\|\cdot\|_{\alpha'}$, but at least an estimate $|\cdot|_{\alpha'} \leq \|\cdot\|_{\alpha'}$ holds (see [3, p. 177]), known as the Hausdorff–Young inequality. For $\alpha' > 2$, the Hausdorff–Young inequality is no longer true, and usage of the norms $|\cdot|_{\alpha'}$ would then appear rather airy.

COROLLARY 4.3. *With the same hypothesis as in Corollary 4.2, let $\hat{g}_k = \mathcal{O}(|k|^{-1})$, and suppose $h(x)$ is essentially bandlimited.*

4. If $1 < \alpha' < \frac{4}{3}$, then $|p - \mathcal{S}_{K,Wp}|_{\alpha'} = \mathcal{O}(m^{\frac{3\alpha'-4}{4\alpha'-4}}) \rightarrow 0$.
5. If $1 < \alpha' < 2$, then $|p - \mathcal{S}_{K,Wp}|_{\alpha'} = \mathcal{O}(b^{\frac{\alpha'-1}{\alpha'}} m^{\frac{1}{2}-\frac{1}{\alpha'}})$.

Proof. We have to go through the proof of Theorem 4.1 with the norm $\|\hat{p} - (\mathcal{S}_{K,Wp})\|_{\alpha}$ as in (4.5), (4.6), but with different $\alpha > 2$. We estimate on the domains Γ_1, Γ_2 . Now according to (4.12),

$$\|\chi_{\Gamma_2} \hat{p}\|_{\alpha} \leq \|\hat{p}\|_{\infty}^{1-2/\alpha} \|\chi_{\Gamma_2} \hat{p}\|_2^{2/\alpha} \leq C \|\mathcal{H}_b h\|_{W^{2,-\frac{1}{2}}}^{2/\alpha},$$

which decays exponentially, since h is essentially bandlimited. So we are left with the error estimate on Γ_1 involving the error terms for g .

Proceeding as in part 8 of the proof of Theorem 4.1, we obtain

$$\|\chi_{\Sigma_1} \hat{p}\|_{\alpha}^{\alpha} \leq C \sum_{|k| \geq m} (|k| - m) \left(R_{(1-\vartheta')|k|}(g) + \|g\|_2 e^{-\gamma|k|} \right)^{\alpha} = \mathcal{O} \left(\sum_{\nu=1}^{\infty} \nu R_{(1-\vartheta')(\nu+m)}(g)^{\alpha} \right),$$

the exponentially decaying term being negligible. Now obviously $\hat{g}_k = \mathcal{O}(|k|^{-1})$ implies $R_{(1-\vartheta')|k|}(g) = \mathcal{O}(|k|^{-1/2})$, so for $\alpha > 4$,

$$\sum_{\nu=1}^{\infty} \nu R_{(1-\vartheta')(\nu+m)}(g)^{\alpha} = \mathcal{O} \left(\sum_{\nu=1}^{\infty} \nu(\nu+m)^{-\alpha/2} \right) = \mathcal{O}(m^{2-\alpha/2}) \rightarrow 0,$$

giving $|p - \mathcal{S}_{K,Wp}|_{\alpha'} = \mathcal{O}(m^{1-\alpha/4})$, which is estimate 4. Finally, if only $\alpha > 2$, we still have $\sum_{\nu} R_{(1-\vartheta')(\nu+m)}(g)^{\alpha} = \mathcal{O}(m^{1-\frac{\alpha}{2}})$, which readily gives estimate 5. This completes the proof. \square

The principal message of Theorem 4.1 and its corollaries is that the aliasing error associated with a choice of the bowtie region (4.3) may be attributed to two different sources. The errors on the regions Σ_2, Σ_3 (resp., Γ_2) decay exponentially (as $b \rightarrow \infty$) if $h(x)$ is essentially bandlimited. On the other hand, the error contribution from Σ_1 , and correspondingly, from Γ_1 , entirely depends on g and no longer relates to the spatial bandwidth b . This error contribution decays as $m \rightarrow \infty$, but in general much slower than the other error terms. In practice, this may require choosing a rather large m , which may render an appropriate sampling difficult (cf. Figure 4). In detail, we have the following observations.

Remarks. (1) If g is of class $\mathcal{C}_{\text{per}}^{\infty}$ or even analytic, the error from region Σ_1 , and hence the overall aliasing error, decays rapidly as the support region K grows. This is of course the case when the source is static, so we reproduce Natterer’s estimates in [20, Thm. III.3.1]. Similarly, if $g(t)$ presents a full dynamic profile, starting with 0 activity, reaching its peak after uptake, and decaying back to 0 after washout, we may realistically assume that $g((T/2\pi)\phi) \in \mathcal{C}_{\text{per}}^{\infty}$, which again gives a fast decay as $m \rightarrow \infty$.

(2) In many practical cases, however, $g((T/2\pi)\phi)$ is not even of class \mathcal{C}_{per} . For instance if only a washout profile is scanned, we usually find $g(t)$ decaying like an exponential or a sum of exponentials, so $g((T/2\pi)\phi)$ is piecewise analytic but discontinuous. Here Theorem 4.1 and Corollary 4.2 are not applicable, since the Fourier coefficients of $g(t) = e^{-\lambda t}$ are $\hat{g}_k = \mathcal{O}(|k|^{-1})$. In this case, we have to retreat to the estimate 4 from Corollary 4.3, which is not entirely satisfactory, as it involves a norm $|\cdot|_{\alpha'}$ with $1 < \alpha' < 2$. One may very well argue that failure of 2-norm convergence indicates a problem in practice, and some of our experiments seem to emphasize this (cf. Figure 4).

(3) Notice that $\hat{g}_k = \mathcal{O}(|k|^{-2})$ if, according to the terminology of [3], g satisfies a *generalized Lipschitz condition of order 2*, that is, if

$$(4.19) \quad g(\phi + h) + g(\phi - h) - 2g(\phi) = \mathcal{O}(h^{-2}) \quad \text{as } h \rightarrow 0,$$

uniformly in $\phi \in [0, 2\pi]$.

(4) The first 2-D Fourier analysis of the unattenuated Radon transform was presented in [22]. These authors calculate the spectrum of a point source $f(x) = \delta(x - a)$. Following their idea, one might consider a *dynamic point source*

$$(4.20) \quad f(t, x) = g(t) \delta(x - a)$$

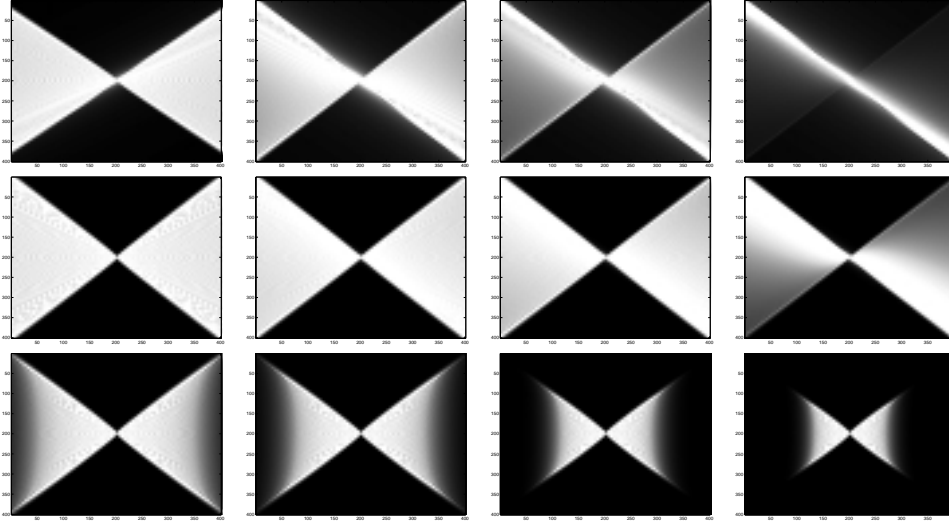


FIG. 3. The first two lines show the effect of the dynamic $g(t) = e^{-\lambda(2\pi/T)t}$ on a point source located at $a = (0.56, 0.8285) \in D$. The first line displays the cases $\lambda = 0.1, 0.4, 0.6$, and 1.1 (left to right). For a fast decay, the spectrum tends to emphasize a diagonal with slope related to the position a of the source. The second line shows the energy spectra for the same dynamics, but after doubling the data. The third line shows the effect of the spatial bandwidth b . This may be simulated by considering sources of the form $h(x) = \phi_{a,\sigma}(x)$ with $g \equiv 1$, where $\phi_{a,\sigma}$ denotes the 2-D Gaussian with mean $a = (0.56, 0.8285) \in D$ and covariance matrix $\sigma^2 I_2$ for different $\sigma = 0.008, 0.01, 0.015$, and 0.02 (left to right). For σ not exceedingly large, $\phi_{a,\sigma}$ may be considered as compactly supported. Notice that $R\phi_{a,\sigma}(s, \omega) = \phi_{a \cdot \omega^\perp}(s)$ is a 1-D Gaussian, whose spectrum may be calculated analytically, cf. [15].

located at $a \in D$ and emitting with dynamic profile $g(t)$. In fact, the energy spectrum of (4.20), while obviously not bounded in σ -direction, still decays on the region Σ_1 (as $m \rightarrow \infty$). This leads to a support region of infinite bowtie shape (see Figure 3). The point of view adopted by considering sources (4.20) is useful since it directly relates the thickness of the bowtie at $\sigma = 0$ to the dynamic profile $g(t)$.

(5) The analysis presented in Theorem 4.1 breaks down at an early stage when R is replaced by the attenuated Radon transform. Even the Fourier slice theorem is no longer available, nor has it an equally useful alter ego. This seems to limit the analysis to numerical experiments, which is of course not entirely satisfactory. Fortunately, adopting the point of view expounded in remark 4, we may interpret attenuation as a particular type of dynamics. In fact, consider a dynamic point source (4.20) located at a and attenuated through $\mu(x)$. Define the function $g_a(\phi)$ by

$$g_a(\phi) = \exp \left\{ - \int_0^\infty \mu(a + \tau\omega) d\tau \right\}, \quad \omega = (\cos \phi, \sin \phi).$$

The attenuated Radon transform of $\delta(\cdot - a)$ is

$$\begin{aligned} R[\mu, \delta(\cdot - a)](s, \phi) &= \int_{-\infty}^\infty \delta(s\omega^\perp + \tau\omega - a) \exp \left\{ - \int_\tau^\infty \mu(s\omega^\perp + \tau'\omega) d\tau' \right\} d\tau \\ &= \exp \left\{ - \int_{a \cdot \omega}^\infty \mu(s\omega^\perp + \tau'\omega) d\tau' \right\} \delta(s - a \cdot \omega^\perp) \\ &= g_a(\phi) \delta(s - a \cdot \omega^\perp) = g_a(\phi) R\delta(\cdot - a)(s, \phi). \end{aligned}$$

Therefore, for a single camera head, according to (3.1), the sinogram of (4.20) is

$$(4.21) \quad p(s, \phi) = g((T/2\pi)\phi) g_a(\phi) R \delta(\cdot - a)(s, \phi).$$

The interpretation of (4.21) is that on a static point source, attenuation acts like a dynamic, while for a dynamic point source, it modulates the existing dynamics. The important point, however, is that as long as 360 degrees are scanned, $g_a(\phi)$ is smooth (as soon as $\mu(x)$ is). Therefore, one may argue that modulating the existing dynamics will not seriously slow down the convergence of the Fourier series, and attenuation will not qualitatively alter the shape of the infinite bowtie support region of the dynamic point source with profile $g(t)$. This seems to be corroborated by numerical experiments.

(6) Notice that a result similar to Theorem 4.1 and Corollary 4.2 may be obtained on a 180-degree tour. The estimates involving Bessel functions have to be modified, but the coefficients replacing $J_n(\theta n)$ still decay exponentially. What makes a 180-degree tour seem more delicate is the more serious effect of attenuation. Namely, $g_a(\phi)$, defined on $[0, \pi]$, and continued periodically outside, will now just like $g((T/\pi)\phi)$ have a discontinuity at $\phi = 0$, adding to the effect of the discontinuity of $g((T/\pi)\phi)$ at $\phi = 0$. Doubling the data in the way shown in the next section will partially remedy this (see Figure 4).

5. Experiments. While the results in the previous section serve to theoretically justify the choice of a frequency window of bowtie shape, K , they do not readily indicate how to calculate K (or rather, m and b) in practice. To do this, we have to provide a practical guideline. Treating the error contributions from Σ_1 and Σ_2, Σ_3 separately, we propose the following approach.

For a dynamic profile $g(t)$ having $\hat{g}_k = \mathcal{O}(|k|^{-\rho})$ for some $\rho > 1$, and for a point source $\delta(\cdot - a)$ located on the unit disk D , consider the spectrum \hat{p} of the sinogram p of $f(t, x) = g(t) \delta(x - a)$. For every frequency σ choose indices $\underline{m}(\sigma)$ and $\overline{m}(\sigma)$ such that

$$(5.1) \quad \sum_{\nu=\underline{m}(\sigma)}^{\overline{m}(\sigma)} |\hat{p}_\nu(\sigma)|^2 \geq .98^{\frac{1}{2}} \cdot \sum_{\nu=-\infty}^{\infty} |\hat{p}_\nu(\sigma)|^2,$$

uniformly over $a \in D$, which is to say that on each line $\sigma = \text{const}$, $[\underline{m}(\sigma), \overline{m}(\sigma)]$ captures 98.99% of the energy of $\hat{p}(\sigma, \cdot)$ (notice $.9899 = .98^{\frac{1}{2}}$). This procedure will, if successful for a given dynamic $g(t)$, provide an infinite region which essentially captures the energy of the spectrum \hat{p} of any source of the form $f(t, x) = g(t) h(x)$, $h(x)$ supported on D , but not necessarily bandlimited. It is hoped that the *same* region will then emerge for a large variety of dynamic profiles $g(t)$.

As it turns out, this program is indeed realizable. Numerical experiments indicate that the desired infinite support region is an infinite bowtie as displayed in Figure 3, with a symmetry $\underline{m} = -\overline{m}$ apparent. In (4.3), the choice $\vartheta \approx 1$ seems justified, and for a large variety of profiles $g(t)$, the delimiters \underline{m} , \overline{m} are then of the form

$$\overline{m}(\sigma) = |\sigma| + m, \quad \underline{m} = -\overline{m},$$

where $m = \overline{m}(0) > 0$ may be calculated explicitly through (5.1).

In a second step we now have to truncate the infinite bowtie at $\sigma = \pm b$ in order to define a bounded region K . This may be done by applying the same argument

again, i.e., by choosing b to satisfy

$$(5.2) \quad \sum_{\nu=\underline{m}(\sigma)}^{\overline{m}(\sigma)} \int_{|\sigma| \leq b} |\hat{p}_\nu(\sigma)|^2 d\sigma \geq .98^{\frac{1}{2}} \cdot \sum_{\nu=\underline{m}(\sigma)}^{\overline{m}(\sigma)} \int_{\mathbf{R}} |\hat{p}_\nu(\sigma)|^2 d\sigma$$

uniformly over $a \in D$. Clearly this step may require a discretization, conveniently done by FFT 2. The combined procedure (5.1), (5.2) specifies a region K carrying 98% of the energy of the spectrum \hat{p} .

A second and easier way to specify a bowtie (4.3) is to discretize the spectrum \hat{p} into a frame of size $S \times S$, say, and then find a tolerance $\epsilon > 0$ to the effect that within the chosen frame, $\hat{p}\chi_{\{|\cdot| \geq \epsilon\}}$ carries 98% of the energy of \hat{p} . Both procedures turn out to be in good agreement, which reinforces the choice (4.3).

Let us now consider an application with experimental data, exhibiting the typical problem with a discontinuous time profile. The study shown in Figure 4 uses a phantom built at Vancouver General Hospital [4] and was performed with a Siemens Multispect-3 (MS3) triple head camera with a low energy ultra high resolution (LEUHR) collimator. Only data from one of the camera heads were used to simulate the case of a single head camera.

The phantom, a 17-ml container shown in Figure 4(a), is connected to a supply and a drain and equipped with a mixing propeller to guarantee a homogeneous flow. The container was initially filled with Tc-99 m of approximately 40 MBq radio activity. The activity was diluted and washed out through uniform water flow, producing approximately a single exponential decay with estimated half-life of 3 minutes. The plot of the total activities of the 64 views of a slice selected at the horizontal pixel position 38 is shown in Figure 4(b). The sinogram of the selected slice is shown in (c), indicating that 180 degrees have been scanned with 64 stops and a camera cross section divided into 64 bins. The time for the total scan was $T = 10$ minutes.

Figure 4(d) shows the energy spectrum of Figure 4(c), obtained via zero filling into a 400×400 frame, applying the 2-D FFT, taking absolute values, and rearranging the image so that high frequencies are at the edges.

The energy spectrum Figure 4(d), expected to resemble a bowtie shape, is blotted by a high energy band in vertical direction. According to theory, this high energy band should not exist here—unless some of the hypothesis on which the results in section 4 are based turned out to be violated. As a list of possible explanations we offer the following.

- (1) The sinogram, being blurred by attenuation and scatter, may contain noise components not modeled in (3.2), whose spectra contribute to the vertical band.
- (2) The bowtie region (4.3) was obtained under the hypothesis that the object is contained in the unit disk. While this is the case for the selected slice, we have to remember that the radiating object is 3-D, and neighboring slices contribute to the data through scatter and collimator blurring. Some of these recorded events may be mistaken as coming from outside the unit circle.
- (3) The problem evoked before: the recorded data present a washout with approximately single exponential decay, see Figure 4(b), causing a discontinuity of $g((T/\pi)\phi)$ at $\phi = 0$. The high energy band visible in Figure 4(d) may indicate the failure of convergence of the Fourier series at $\phi = 0$, or rather, that a very large $m = \overline{m}(0)$ is required in (5.1).

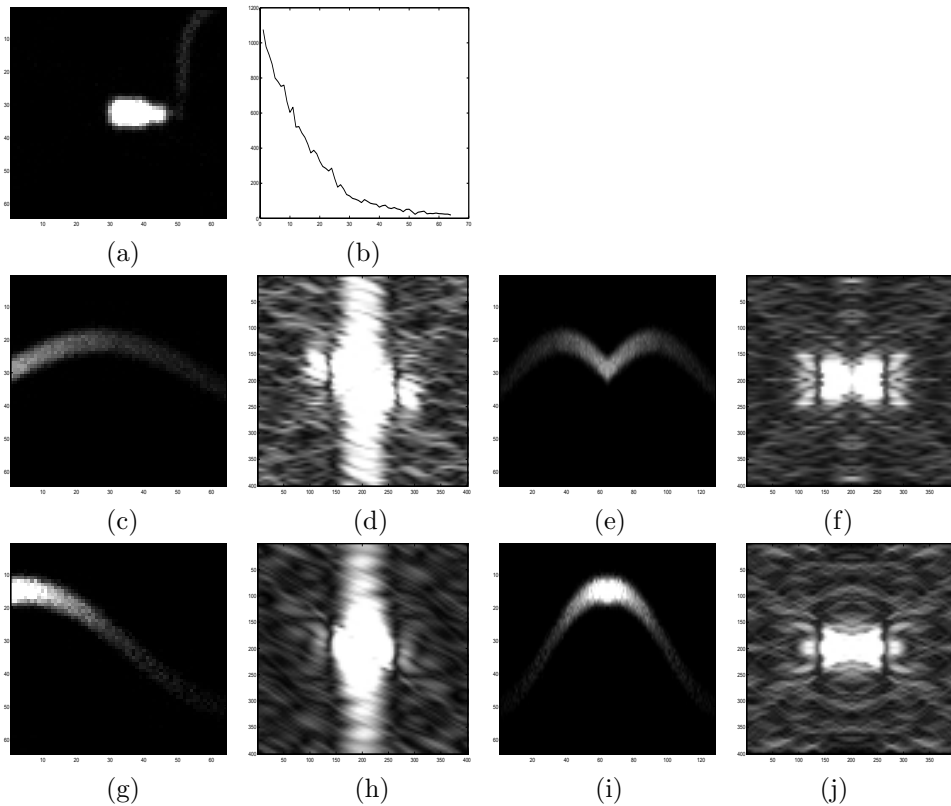


FIG. 4. *Experimental data from Vancouver General Hospital, obtained with a Siemens Multispect-3 triple head camera.*

- (4) Since a 180-degree sector has been scanned, the sinogram, along with the discontinuity in time, has a singularity in the spatial variable, visible in Figure 4(e) as a kink, which may as well be responsible for the phenomenon.

In order to decide which of these items is likely to cause the phenomenon of Figure 4(c), we *double* the data by flipping the sinogram with respect to the axis $\phi = 0$, including the reverse data among a new symmetric sinogram of size 128×64 , displayed in Figure 4(e). The doubled sinogram now has an increase of activity on $[-\pi, 0]$, followed by the original period of decay on $[0, \pi]$.

The effect of the doubling procedure, while theoretically improving the signal to be of class $\mathcal{C}_{\text{per}}(-\pi, \pi)$, is dramatic in the case of our experiment. The energy spectrum Figure 4(f) of the doubled sinogram no longer exhibits the erratic vertical energy band and quite reasonably displays the bowtie form predicted by theory. As the decay profile of the bottle may very well be approximated by an exponential $e^{-\lambda\phi}$, the doubling procedure may even theoretically be justified. While the Fourier coefficients of $e^{-\lambda\phi}$ are $\mathcal{O}(|k|^{-1})$, the doubled signal $e^{-\lambda|\phi|}$ on $[-\pi, \pi]$ has Fourier coefficients $c_k = (1 + (-1)^{k+1}e^{-\lambda\pi}) \frac{2\lambda}{\lambda^2 + k^2} = \mathcal{O}(|k|^{-2})$. In any case, we strongly recommend the doubling procedure, particularly if the dynamic is relatively fast.

In order to indicate that the phenomenon in Figure 4(d) is not due to any of the noise effects evoked in items (1) and (2) of our list, one may create an artificial 2-D object, resembling the true slice of the bottle, with activity distribution a properly

scaled 2-D Gaussian. For the dynamics one would substitute a single exponential decay found by inspecting the cumulative activity plot Figure 4(b). The result, not displayed here, shows that the Gibbs phenomenon is still apparent, reinforcing our explanation (3).

Finally, to discriminate item (3) from the possible explanation (4), we have scanned the bottle from a different position (Figure 4(a)), the sinogram of the corresponding slice shown in Figure 4(g), and selected to the effect that in the doubled sinogram in Figure 4(i) the spatial singularity is removed. The energy spectra in Figure 4(h), belonging to in Figure 4(g), and in Figure 4(j), belonging to Figure 4(i), show that the result is qualitatively the same, indicating that the phenomenon (4) is less serious than (3).

6. Resolution. We present the promised guideline on how to acquire data with a rotating SPECT camera. Consider exemplarily the case of a single camera head rotating over a 180-degree tour. Doubling the data will then give a 360-degree sinogram. Suppose the dynamic source $f(t, x)$ is of the form $g_1(t) h_1(x) + \dots + g_r(t) h_r(x)$, with the $h_i(x)$ supported on the unit disk. Assume that the unit circle is completely visible from each camera position, which means that a camera cross section has length 2. Assume that the cross section is divided into 64 bins, giving $\Delta s = 1/32$. Since the Nyquist rate is $\Delta s = \pi/b$, the best possible bandwidth is $b = 32\pi$, a fact we may not easily debate if the resolution of the camera has to be considered a fixed technical parameter.

According to (4.4), the sampling parameters in the frequency plane are $\Delta\sigma = b$, $\Delta k = [b] + 2m$, where we have chosen $\vartheta \approx 1$, as validated by the numerical experiments in section 4. Using (4.4), this gives

$$(6.1) \quad \Delta s = \frac{\pi}{b}, \quad \Delta\phi = \frac{\pi}{[b] + 2m}.$$

Let us consider the case where a washout (with decreasing activity) is scanned. As it comes out, tracer dynamics are often described by a *compartmental model* (cf. [11]), and accordingly the dynamic source is represented as a sum of exponentials

$$f(t, x) = h_1(x) e^{-\lambda_1(\pi/T)t} + \dots + h_r(x) e^{-\lambda_r(\pi/T)t}$$

with $\lambda_i \geq 0$ (decay to 0 at infinity) and where the $h_i(x)$ are supported on the unit disk D . In practice we may usually exhibit $\lambda_i \leq \lambda$, the fastest dynamic to be expected. Then the bowtie region may be estimated by considering a source of the form $f(t, x) = h(x) g(t) = h(x) e^{-\lambda(\pi/T)t}$.

As $g((T/\pi)\phi) = e^{-\lambda\phi}$, doubling the data as suggested in our approach gives the dynamic profile $e^{-\lambda|\phi|}$ over $-\pi \leq \phi \leq \pi$. Estimating the thickness $m = m(\lambda)$ of the bowtie as a function of λ , based on (5.1), yields the approximate linear relationship

$$(6.2) \quad m(\lambda) \approx \frac{3}{8} \lambda + 1,$$

which we exploit a little further by considering a realistic situation comparable to the one in our experiment.

Suppose that the total acquisition time of the scan is $T = 10$ minutes, while the shortest expected half-life is of the order of 2 minutes. Then $t_{\frac{1}{2}} = T \log 2/\pi\lambda = .2T$, giving $\lambda = \log 2/.2\pi \approx 1.1$. Hence $g((T/\pi)\phi) = \exp\{(-\log 2/.2\pi)|\phi|\} = \exp\{-1.1|\phi|\}$, which through (6.2) suggests $m \approx 1.4$. In view of (6.1), this gives $\Delta\phi \approx .06 = 3.44$

degrees as satisfactory for practical purposes. The interpretation is that an appropriate sampling of the doubled signal over 360 degrees requires approximately 105 views, that is, 53 views over 180-degrees. This is not in complete agreement with the actual policies (cf. [16]), where we often prefer to take 64 views on a 180-degree tour. As our scenario ignores the noise contributions, 53 views may in practice be barely sufficient, and we consider 64 views as a practical guideline on 180 degrees.

Remark. Formula (6.1) may be interpreted as an *uncertainty principle*. Assume that a minimum $\Delta\phi$ has been specified by the user to guarantee a sufficient number of recorded counts per camera position. Then we may consider $[b] + 2m$ as fixed. So within certain limits, we may either increase m and capture faster dynamics, paying eventually by a loss in spatial resolution (by decreasing b), or we may conversely choose a better spatial resolution by increasing b , bearing the risk that some of the faster dynamics may not be adequately represented.

7. Filtering. In this last section we discuss a policy for the 2-D filtering of the sinogram data. Notice that filtering of the projection data is currently done in one dimension, that is, every projection is filtered separately. In the static case, this does not cause any particular difficulty, as the same filter may be used for all projections. To that effect, various filters have been around for years, and their application is well understood.

The situation is a little more complicated in dSPECT, as the overall activity changes from view to view. 1-D filtering may now require adapting an individual filter to each projection, and it may then seem more attractive to do a 2-D filtering, based on the insights of section 4. In particular, a 2-D filter, if based on the 2-D Fourier transform, may use the bowtie shape of the spectrum of the Radon transform, and may therefore incorporate information not easily assessed through a 1-D procedure. We therefore propose the following frequency domain based 2-D filtering procedure, which incorporates the theoretical results obtained in previous sections.

To render the situation even more interesting, we modify the experiment from section 5 by scanning four bottles of the type shown in Figure 4(a). We arrange a washout through continuous water flow of different half-lives between 2 and 6 minutes. Starting out with the 64×64 sinogram (Figure 5, top left), we double data (top row right) as done previously, and include them into a frame of zeros of considerably larger size $L \times L$ (zero filling), where usually $L = 200$ or $L = 400$. The 2-D FFT is applied to the enlarged signal. Filtering is now performed in the frequency domain by multiplying the $L \times L$ spectrum with a 2-D window function:

$$w_{m,b}(x,y) = \phi(x/b)\phi(y/(m+x))$$

with $-L/2 \leq x, y \leq L/2$ integer and parameters $m, b \leq L/2$. The window function satisfies $\phi(0) = 1$, $\phi(t) = 0$ for $|t| \geq 1$ and could be any of the standard 1-D lag windows. Figure 5 (second row) displays several filters with the choice $L = 200$, b ranging from 100 to 70, and m ranging from 80 to 20.

Rows 3–6 show the effect of the 2-D filtering of these window functions. The left-hand picture shows three projections (number 4, number 19, and number 61). The dotted line shows the original data, the continuous line shows the filtered curves. The right-hand diagram shows the smoothing effect of the filters on the sum plot. The latter indicates the success of the doubling, as the same filtering applied to the simple sinogram would exhibit a Gibbs phenomenon at $\phi = 0$.

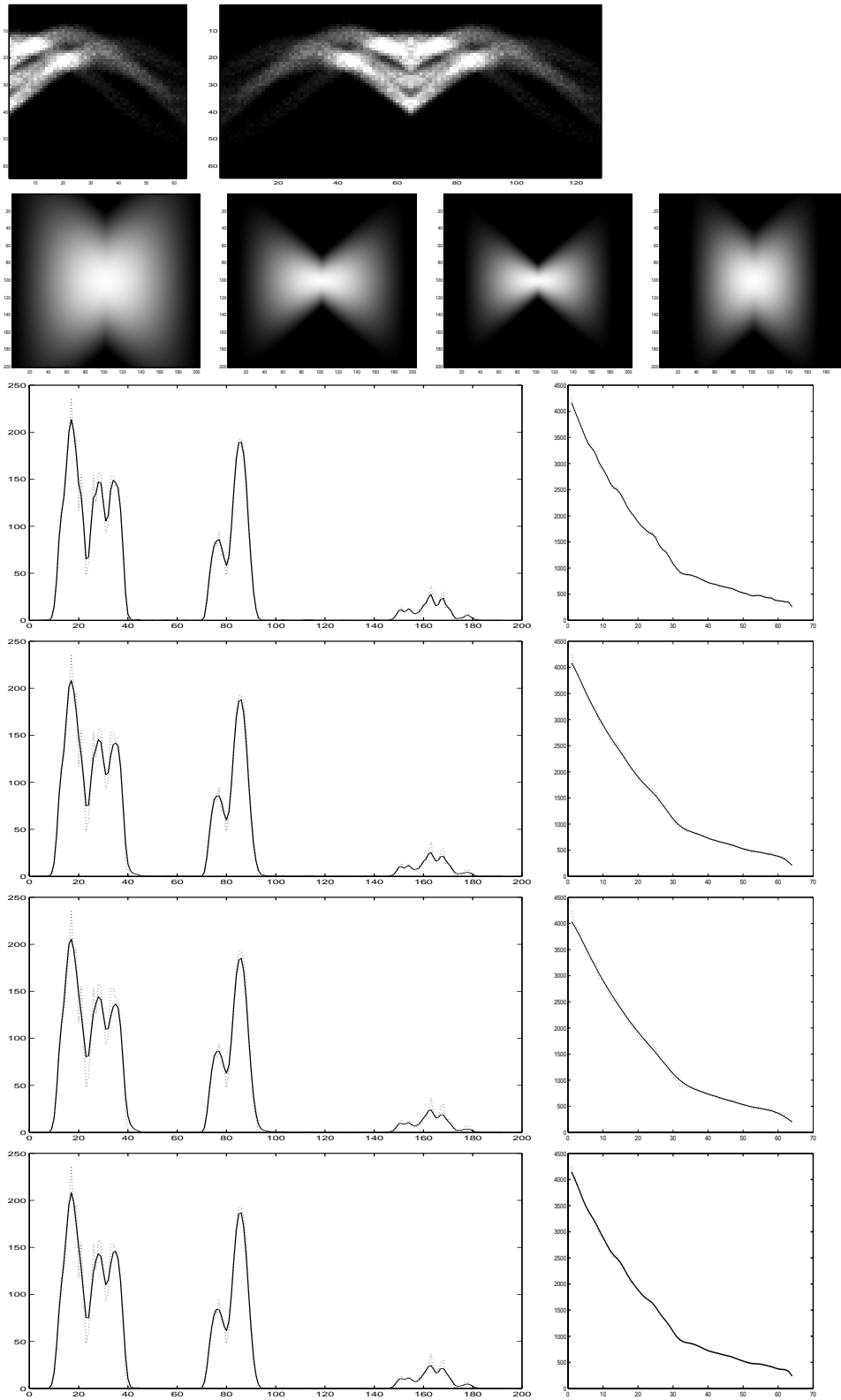


FIG. 5. 2-D filtering of experimental data.

REFERENCES

- [1] M. ABRAMOWITZ AND I.A. STEGUN, *Handbook of Mathematical Functions*, Dover, New York, 1970.
- [2] H.H. BAUSCHKE, D. NOLL, A. CELLER, AND J.M. BORWEIN, *An EM-algorithm for Dynamic SPECT Tomography*, IEEE Trans. Med. Imag., 18 (1999), pp. 252–261.
- [3] P.L. BUTZER AND R.J. NESSEL, *Fourier Analysis and Approximation*, Vol. 1, Birkhäuser-Verlag, Basel, 1971.
- [4] A. CELLER, T. FARNCOMBE, R. HARROP, AND D. LYSTER, *Dynamic heart-in-thorax phantom for functional SPECT*, IEEE Trans. Nuclear Sciences, 44 (1997), pp. 1600–1605.
- [5] A. CELLER, T. FARNCOMBE, R. HARROP, D. NOLL, AND J. MAEGHT, *Dynamic SPECT imaging using single camera rotation (dSPECT)*, IEEE Trans. Nuclear Sciences, 46 (1999), pp. 1055–1061.
- [6] A. CELLER, A. SITEK, AND R. HARROP, *Reconstruction of multiple line source attenuation maps*, in IEEE Nuclear Science Symposium Conference Record, IEEE, New York, 1996, pp. 1420–1424.
- [7] A. CELLER, A. SITEK, E. STOUB, D. LYSTER, C. DYKSTRA, D. WORSLEY, AND A. FUNG, *Development of a multiple line source attenuation array for SPECT transmission scans*, J. Nuclear Medicine, 38 (1997), p. 215.
- [8] R. DAUTREY AND J.-L. LIONS, *Analyse mathématique et calcul numérique*, Tome 9, Masson, Paris, 1984.
- [9] V. DICKEN, *Simultaneous activity and attenuation reconstruction in emission tomography*, Inverse Problems, 15 (1999), pp. 931–960.
- [10] G.T. GULLBERG, R.H. HUESMAN, S.G. ROSS, E.V.R. DI BELLA, G.L. ZENG, B.W. REUTTER, P.E. CHRISTIAN, AND S.A. FORESTI, *Dynamic cardiac single photon emission computed tomography*, in Nuclear Cardiology: State of the Art and Future Directions, Mosby-Year Book, Philadelphia, in press.
- [11] A. GJEDDE, *Compartmental Analysis*, in Principles of Nuclear Medicine, 2nd ed., H.N. Wagner, Jr., Z. Szabo, J.W. Buchanan, Saunders, Philadelphia, PA, 1995, pp. 451–461.
- [12] C.M. KAO, J.T. YAP, J. MUKHERJEE, M. COOPER, AND C.T. CHEN, *An image reconstruction method for dynamic PET*, IEEE NSS/MIC Conference Record, IEEE, New York, 1995.
- [13] H. KRUSE, *Resolution of reconstruction methods in computerized tomography*, SIAM J. Sci. Stat. Comput., 10 (1989), pp. 447–474.
- [14] M.A. LIMBER, M.N. LIMBER, A. CELLER, J.S. BARNEY, AND J.M. BORWEIN, *Direct reconstruction of functional parameters for dynamic SPECT*, IEEE Trans. Nuclear Sciences, 42 (1995), pp. 1249–1256.
- [15] A. KURUC, *Efficient estimation of linear functionals in emission tomography*, SIAM J. Appl. Math., 57 (1997), pp. 426–452.
- [16] J. MAEGHT, D. NOLL, A. CELLER, AND T. FARNCOMBE, *Methods for dynamic SPECT*, Rapport Interne 99-26, Laboratoire Mathématiques pour l’Industrie et la Physique, 1999. Also available at <http://mip.ups.-tlse.fr/publi>.
- [17] K. NAKAJIMA, J. TAKI, H. BUNKO, M. MATSUDAIRA, A. MURAMORI, I. MATSUNARI, K. HISADA, AND T. ICHIHARA, *Dynamic acquisition with a three-headed SPECT system: Application of Technetium 99m-SQ30217 myocardial imaging*, J. Nuclear Medicine, 32 (1991), pp. 1273–1277.
- [18] F. NATTERER, *Computerized tomography with unknown sources*, SIAM J. Appl. Math., 43 (1983), pp. 1201–1212.
- [19] F. NATTERER, *Sampling in fan beam tomography*, SIAM J. Appl. Math., 53 (1993), pp. 358–380.
- [20] F. NATTERER, *The Mathematics of Computerized Tomography*, Teubner-Verlag, Stuttgart, 1986.
- [21] F. NATTERER, *Determination of tissue attenuation in emission tomography of optically dense media*, Inverse Problems, 9 (1993), pp. 731–736.
- [22] P.A. RATTEY AND A.G. LINDGREN, *Sampling the 2-D Radon transform*, IEEE Trans. Acoust. Speech Signal Process., 29 (1981), pp. 994–1002.
- [23] G.N. WATSON, *A Treatise on Bessel Functions*, Cambridge University Press, Cambridge, UK, 1952.
- [24] A. WELCH, R. CLARK, F. NATTERER, AND G.T. GULLBERG, *Toward accurate attenuation correction in SPECT without transmission measurements*, IEEE Trans. Med. Imag., 16 (1997), pp. 532–541.
- [25] R.G. WELLS, A. CELLER, AND R. HARROP, *Analytic calculation of photon distribution in SPECT projections*, IEEE Trans. Nuclear Sciences, 45 (1998), pp. 3202–3214.